ACSNANO

www.acsnano.org

ARTICLE

Phonon and Thermal Properties of Quasi-Two-Dimensional $FePS_3$ and $MnPS_3$ Antiferromagnetic Semiconductors

Fariborz Kargar,*,# Ece A. Coleman,# Subhajit Ghosh, Jonathan Lee, Michael J. Gomez, Yuhang Liu, Andres Sanchez Magana, Zahra Barani, Amirmahdi Mohammadzadeh, Bishwajit Debnath, Richard B. Wilson, Roger K. Lake, and Alexander A. Balandin*

Cite This: *ACS Nano* 2020, 14, 2424–2435

Read Online

ACCESS | Metrics & More | Article Recommendations | Supporting Information

ABSTRACT: We report results of investigation of the phonon and thermal properties of the exfoliated films of layered single crystals of antiferromagnetic $FePS_3$ and $MnPS_3$ semiconductors. Raman spectroscopy was conducted using three different excitation lasers with wavelengths of 325 nm (UV), 488 nm (blue), and 633 nm (red). UV−Raman spectroscopy reveals spectral features which are not detectable *via* visible Raman light scattering. The thermal conductivity of $FePS_3$ and $MnPS_3$ thin films was measured by two different techniques: the steady-state Raman optothermal and transient time-resolved magneto-optical Kerr effect. The Raman optothermal measurements provided the orientation-average thermal conductivity of $FePS_3$ to be 1.35 ± 0.32 W m^{-1} K^{-1} at room temperature. The transient measurements revealed that the through-plane and in-plane thermal conductivity of $FePS_3$ are 0.85 ± 0.15 and 2.7 ± 0.3 W m^{-1} K^{-1}, respectively. The films of $MnPS_3$ have higher thermal conductivity of 1.1 ± 0.2 W m^{-1} K^{-1} through-plane and 6.3 ± 1.7 W m^{-1} K^{-1} in-plane. The data obtained by the two techniques are in agreement and reveal strong thermal anisotropy of the films and the dominance of phonon contribution to heat conduction. The obtained results are important for the interpretation of electric switching experiments with antiferromagnetic materials as well as for the proposed applications of the antiferromagnetic semiconductors in spintronic devices.

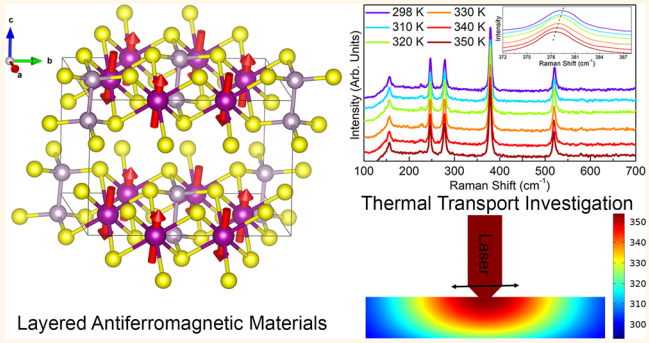

KEYWORDS: *antiferromagnetic semiconductors, quasi-2D materials, Raman spectroscopy, thermal conductivity, spintronics*

Transition-metal phosphotrichalcogenides, MPX_3, where M is a transition metal, *e.g.*, V, Mn, Fe, Co, Ni, or Zn, and X is a chalcogenide such as S, Se, or Te, span a wide variety of layered compounds with different electronic, optical, and magnetic properties.[1] Bulk MPX_3 materials have been extensively studied during the last three decades mostly because of their potential application as cathodes in lithium batteries.[2,3] With the beginning of the era of two-dimensional (2D) materials after exfoliation of stable atomically thin single-layer graphene[4] and discovery of its unique electronic[5−7] and thermal properties,[8,9] the attention turned to quasi-2D films of transition-metal dichalcogenides (MX_2) and MPX_3. It has been demonstrated that some MX_2 exhibit ferromagnetic (FM) properties at monolayer thicknesses even at room temperature (RT).[10,11] Motivated by the desire to find intrinsic antiferromagnetic (AFM) ordering in the 2D limit, it was discovered that MPX_3 structures are one of those rare few-layer van der Waals (vdW) materials, which can have stable intrinsic antiferomagnetism even at mono- and few-layer thicknesses.[12]

The existence of weak vdW bonds between the MPX_3 layers makes them a potential candidate for 2D spintronic devices. The "cleavage energy" of these materials—the energy required to separate a crystal into two parts along a basal plane— is close to that of graphite.[13] More specifically, the "cleavage energy" of $FePSe_3$ is slightly higher than that of the graphite, while that for all other combinations of the M and X elements is lower than that of graphite. The Néel temperature, T_N, for

Received: December 15, 2019
Accepted: January 17, 2020
Published: January 17, 2020

https://dx.doi.org/10.1021/acsnano.9b09839
ACS Nano 2020, 14, 2424–2435

$FePS_3$, $MnPS_3$, and $NiPS_3$ is reported to be around 118, 78, and 155 K.[14] The M element determines the type of the phase transition from AFM to paramagnetic (PM) ordering. While $FePS_3$ shows Ising-type phase transition at T_N, $MnPS_3$, and $NiPS_3$ follow Heisenberg- and XY-phase transitions, respectively.[12] The metal element of the MPX_3 materials modifies the band gap from a medium band gap of ∼1.3 eV to a wide band gap of ∼3.5 eV suitable for optoelectronic applications.[13,14] While $FePS_3$ has an indirect bandgap of 1.5 eV, $MnPS_3$ exhibits a direct bandgap of 3.0 eV, respectively.[2,13] The diverse properties of these materials tunable by proper selection and combination of the M and X elements make the MPX_3 materials an interesting platform for fundamental science and practical applications in spintronic devices,[15,16] lithium batteries,[3] field-effect transistors,[17] UV light detectors,[17] thermoelectrics,[18] and photocatalytic systems.[19] The semiconductor nature of $FePS_3$ and $MnPS_3$ and the possibility of electron and phonon band-structure engineering with strain[14] make these materials particularly interesting from the fundamental and practical applications points of view.

The optical phonon properties of $FePS_3$ and $MnPS_3$ bulk crystals have been studied extensively using Raman spectroscopy and infrared (IR) absorption techniques.[12−14,20−30] The early Raman studies of bulk crystals suggested that the vibrational dynamics of both crystals can be pictured within the framework of a molecular approach, dividing the Raman spectrum into the high-frequency internal modes of P_2S_6, and the low-frequency modes where the interaction of the M element with phosphorus (P) and chalcogenides (X) becomes significant. A recent temperature-dependent polarized Raman study of bulk, few-, and monolayer $FePS_3$ revealed features in the spectra, emerging at the transition temperature, and suggested that a monolayer $FePS_3$ possesses an Ising-type AFM ordering.[12] Another Raman study of $MnPS_3$ indicated that $MnPS_3$ exhibits three phase transitions at 55, 80, and 120 K, which were attributed to unbinding of spin vortices, transition from an AFM to a PM state, and two-dimensional spin critical fluctuations, respectively.[22] Although available Raman and IR-absorption studies are in general agreement, there exist ambiguities with peak assignments in the frequency range from 400 to 500 cm^{-1}. Some IR[28] and Raman[25] investigations reported an anomalous peak at ∼480 cm^{-1}. While this peak was assigned to the normal vibration of the P−P bond, the available theoretical reports[31] do not show any optical phonon modes at this frequency. Other experimental studies found the P−P mode peak at ∼430 cm^{-1} as a weak feature in Raman and strong peak in IR-absorption spectroscopy. Since the peak at 480 cm^{-1} exhibits low intensity, and it emerges as a broad shoulder in the visible laser Raman and IR spectra, the nature of these spectral feature has been questioned. In the present study, we report the vibrational dynamics of crystalline thin films of $FePS_3$ and $MnPS_3$ using three different lasers, with the excitation wavelengths of 325 nm (UV), 488 nm (blue), and 633 nm (red). The Raman spectra obtained by blue and red lasers are in excellent agreement with the available literature. The data acquired by UV−Raman spectroscopy are similar for both crystals, revealing an intense peak at ∼467 cm^{-1}. We also report the temperature-dependent and excitation power dependent coefficients for the phonon modes in both material systems. The coefficients are required for understanding the anharmonicity of the crystal lattice and for determining the average thermal conductivity using the optothermal Raman technique.

Although magnetic and electronic properties of the MPX_3 family of compounds have been investigated intensively, there have been no experimental reports on the thermal properties of these materials. Like other layered crystalline materials, the members of the MPX_3 family are expected to have strongly anisotropic thermal properties owing to their weak vdW interlayer bonds and strong in-plane covalent bonds. A recent theoretical study reported an exceptionally low thermal conductivity of monolayer $ZnPSe_3$, which makes it a potential candidate for thermoelectric applications.[18] The knowledge of thermal transport properties of quasi-2D MPX_3 materials is important for spintronic and thermoelectric applications.[16] It has been suggested that AFM materials have advantages over FM materials in spintronic applications, *e.g.*, in spin-Seebeck effect (SSE) devices, since they are less susceptible to external magnetic fields, and possess a linear magnon dispersion in the vicinity of Brillouin zone (BZ) center with a high group velocity.[16] In the AFM based SSE devices,[15] the AFM material can be utilized, instead of FM material, as the spin generation layer. The generated voltage, V, by the SSE device, as a result of the induced temperature gradient, ΔT, by a power source, P, across the AFM layer is inversely proportional to its thermal conductivity, k, *i.e.*, $V \propto \Delta T \propto P/k$. It has been theoretically suggested that polar AFM materials like $MnPS_3$ with honeycomb structure and broken inversion symmetry can be used in SSE devices to act as a nonreciprocal spin transport medium.[32] For these reasons, the knowledge of the thermal properties of MPX_3 materials becomes essential for designing the spintronic devices. In this study, we use the steady-state optothermal Raman and transient time-resolved magneto-optical Kerr effect (TR-MOKE) techniques in order to determine the direction-average, in-plane, and through-plane thermal conductivity values of the exfoliated thin films of the high-quality $FePS_3$ and $MnPS_3$ single crystals.

RESULTS AND DISCUSSION

Commercially available high-quality single crystals of $FePS_3$ and $MnPS_3$ (HQ Graphene) were used for Raman spectroscopy and TR-MOKE experiments. The materials were synthesized using the chemical vapor transport (CVT) method. Figure 1a,b shows the results of X-ray diffraction spectroscopy (XRD) of $FePS_3$ and $MnPS_3$ crystals, respectively. The XRD data reveals that both materials possess a pure single-crystal phase with major (001) and (002) crystallographic planes.[20] The insets in Figure 1a,b illustrate the crystal structure of both material systems where the gray, yellow, gold, and violet spheres represent phosphorus (P), sulfur (S), iron (Fe), and manganese (Mn) atoms, respectively. The red arrows show the direction of the spin ordering in metallic atoms in each layer. The energy-dispersive X-ray spectroscopy (EDX) data confirming the purity of chemical structures of the crystals is presented in Supplementary Figure S1.

The crystals were mechanically exfoliated onto Si/SiO_2 and diamond substrates. The resulting multilayer flakes had lateral dimensions of 5−25 μm. The optical images of the representative flakes are shown in Supplementary Figure S2. The thicknesses of the samples were verified with the atomic force microscopy (AFM) (Supplementary Figure S3). Raman spectroscopy (Renishaw inVia) measurements were performed in the backscattering configuration using three lasers with different excitation wavelengths of 325 nm (UV), 488 nm (blue), and 633 nm (red). In order to avoid self-heating effects,

https://dx.doi.org/10.1021/acsnano.9b09839
ACS Nano 2020, 14, 2424−2435

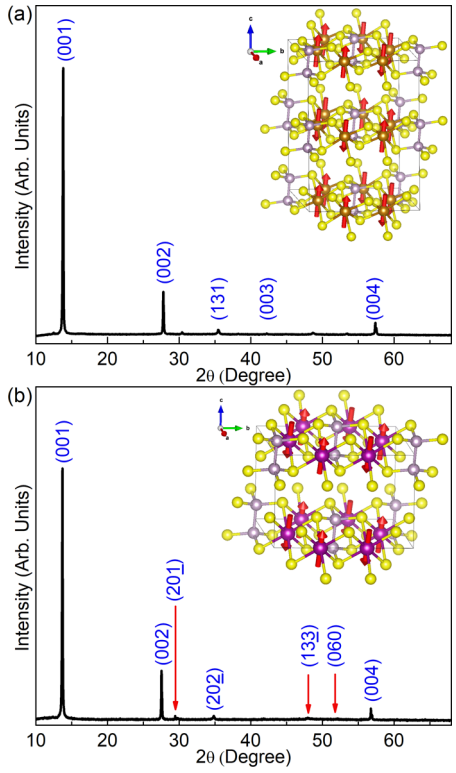

Figure 1. X-ray diffraction (XRD) patterns of high-quality single crystals of (a) $FePS_3$ and (b) $MnPS_3$. Both spectra exhibit intense peaks corresponding to the crystallographic planes of (001) and (002) confirming the high-quality single-crystal structure of the material systems. The insets in (a) and (b) demonstrate the atomic structure of the $FePS_3$ and $MnPS_3$ where the gray, yellow, gold, and violet spheres represent phosphorus (P), sulfur (S), iron (Fe), and manganese (Mn) atoms, respectively. The arrows show the spin ordering of both crystals in antiferromagnetic state.

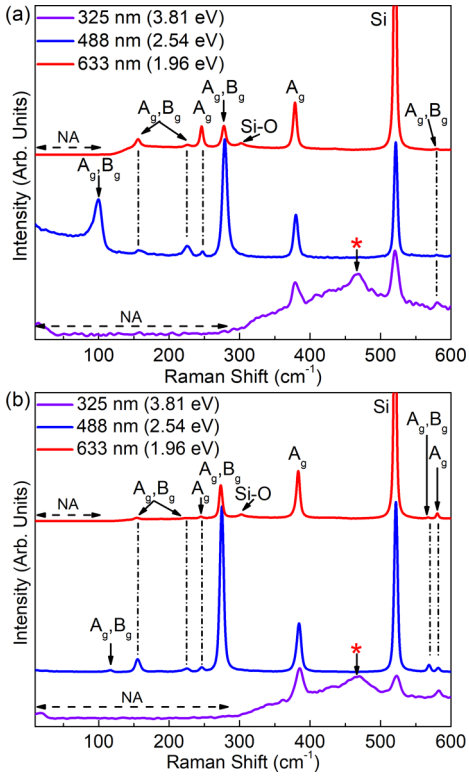

Figure 2. Raman spectroscopy of (a) $FePS_3$ and (b) $MnPS_3$ single crystals at room temperature using three different laser excitations of 325 nm (UV), 488 nm (blue), and 633 nm (red). The results of UV laser excitations exhibit an additional combined peak at ~465 cm^{-1} for both crystals which have not been reported previously. In both panels, the horizontal arrows labeled as "NA" show the inaccessible frequency range due to the Raman filter cutoff frequency at each laser excitation wavelength.

we used low laser excitation power of <100 μW in all experiments.

The RT Raman spectra of $FePS_3$ and $MnPS_3$ on silicon (Si) substrate at three different laser excitations are presented in Figure 2a,b. The Raman-specific filter cutoff frequencies for UV, blue, and red excitation lasers are 300, 10, and 110 cm^{-1}, respectively. The inaccessible frequency range for each excitation laser wavelength is illustrated by horizontal arrows labeled as "NA". The corresponding wavenumbers of the observed peaks are listed in Table 1. In all spectra, the sharp peak at 520 cm^{-1} is originated from the silicon substrate. One can notice similarities in the Raman normal modes for both materials at each laser excitation. The accumulated spectra excited by the blue laser reveal the lowest modes for $FePS_3$ and $MnPS_3$ at 98 and 117 cm^{-1}, respectively. These modes are only detectable by the blue laser as their frequency range is beyond the Raman filter cutoff frequency for the red and UV lasers. Although the MPX_3 structures have a complex atomic configuration, their Raman signatures can be divided into the internal vibrational modes of the ethane-type $P_2S_6^{4-}$ and external vibrational modes of the M^{2+} and $P_2S_6^{4-}$.[26] The higher frequency modes in the spectra of both materials originate from the internal modes of $P_2S_6^{4-}$. Since this is common to both crystals, the associated Raman modes are nearly identical. The bulk MPX_3 crystals belong to the $C_{2/m}$ space symmetry group with the irreducible representation of $\Gamma = 8A_g + 6A_u + 7B_g + 9B_u$ zone-center modes in which only the A_g and B_g modes are active in the regular Raman spectroscopy with the blue and red laser excitation.[26,30] In theoretical calculations of the AFM phase, the number of irreducible representations is doubled by the lower symmetry in the modulated structure and will be discussed in detail later. All Raman peaks obtained under the red and blue laser excitations are in excellent agreement with available literature.[20−30] The Raman spectra obtained under UV laser excitation shows two additional peaks for both crystals, identified by a red star in Figure 2a,b, which are not detectable by visible light Raman spectroscopy.

The UV−Raman spectra of $FePS_3$ and $MnPS_3$ on Si are shown separately in Figure 3a,b. There are four peaks identified as P_i, i = 1...4 in this figure. The peaks marked as P_1 and P_4 are present in the Raman spectra excited by red and blue lasers (Figure 2). The peak P_2 at ~430 cm^{-1} is not detectable by visible Raman spectroscopy. Under UV laser excitation, this spectral feature appears as a low-intensity shoulder. A peak at the same frequency has been reported previously using IR spectroscopy.[28] It was attributed to the zone-center phonon mode with B_u symmetry which is not a regular Raman active mode. There is also a distinguishable broad peak, labeled as P_3, which is detectable only with the UV Raman spectroscopy. As one can see in Figure 3, the P_2 and P_3 features can be fitted accurately using two separate Gaussian peaks (green curves). The spectral position of each individual constituent of the P_3 feature is almost identical for both materials (Table 1). Comparing the experimental UV−Raman

https://dx.doi.org/10.1021/acsnano.9b09839
ACS Nano 2020, 14, 2424−2435

Table 1. Raman Normal Modes of $FePS_3$ and $MnPS_3$ at Different Laser Excitation Wavelengths

		experimental Raman normal modes (cm^{-1})									
	excitation laser	A_g, B_g	A_g, B_g	A_g, B_g	A_g	A_g, B_g	A_g	B_u	2nd order Raman	A_g, B_g	A_g
$FePS_3$	UV	NA[a]					379	431	467		580
	blue	98	158	226	247	279	380				579
	red	NA[a]	156	227	246	278	378				579
$MnPS_3$	UV	NA[a]					385	428	467		582
	blue	117	156	225	246	274	384			568	581
	red	NA[a]	156	226	245	273	383			567	581
	magnetic order	DFT calculated Raman normal modes (cm^{-1})									
$FePS_3$	NM		162	209	250	290	358	417		526	593
			170	220		291					
	AFM	93	161	221	242	276	368	435		544	553
			163	225		277	375			545	554

[a]NA: "not accessible" due to the Raman filter cutoff frequency at that specific laser excitation wavelength.

results with the available theoretical phonon dispersion data,[31] one notices that there is no phonon band, either at the BZ center or at the high-symmetry points of the BZ boundaries, corresponding to the frequencies associated with P_3. We note that somewhat similar spectral features have been reported using IR spectroscopy[28] as low intensity peaks defined as shoulders. Since the experiments were conducted at RT, which is significantly higher than the Néel temperature for both materials, it is unlikely that this spectral feature is associated with the light scattering by one or two magnons. The UV−Raman spectrum of a bare Si substrate, and on different spots of various exfoliated flakes are presented in Supplementary Figures S4−S6, confirming that the observed P_3 peak originates form the MPX_3 crystals themselves. The anomalous P_3 Raman peak is most likely related to the second order Raman scattering of the A_g mode at ~247 cm^{-1}. The scattering cross section for the second order Raman peaks strongly correlates with the incident laser light energy, *i.e.*, the higher the incident photon energy, the higher the second-order scattering cross section. This is why the P_3 peak is present in UV Raman spectrum but not detectable *via* visible-light Raman experiments.[33]

Prior theoretical studies of monolayers[31] find a Raman active normal mode for both crystals between 530 and 550 cm^{-1}. However, as shown in Figures 2a,b, the silicon substrate also shows an intense peak at 520 cm^{-1} which masks Raman features originating from the MPX_3 crystals. To address this issue, UV−Raman measurements were conducted on $FePS_3$ flakes exfoliated on a diamond substrate, and the results are shown in Figure 3c. Comparing the accumulated Raman spectra from the bare diamond substrate (orange curve) and $FePS_3$ on diamond (violet curve) confirms that there are no vibrational modes at 520 cm^{-1} associated with $FePS_3$. The UV−Raman spectroscopy of the bare diamond substrate is shown in Supplementary Figure S7.

In order to elucidate the nature of the two experimentally observed modes between 400 and 500 cm^{-1}, we performed density functional theory calculations of bulk $FePS_3$ as implemented in VASP.[34,35] The schematic representation of the atomic structure of $FePS_3$ is shown in Supplementary Figure S8. Exchange-correlation is included with the Perdew−Burke−Ernzerhof (PBE) functional.[36] A Hubbard-U type correction is applied to the d-orbitals of the Fe atoms using the VASP default model that depends only on the value of $U-J$. A $U-J$ value of 3.5 eV was used for all calculations. van der Waals forces are included with the DFT-D2 method of Grimme.[37] Atomic positions are relaxed until the Hellman−Feynman forces are less than 10^{-4} eV/Å. Total energies are converged to within 10^{-7} eV in both the geometry relaxation and the phonon calculations. Full details of the calculations are provided in the Supporting Information.

The vibrational modes are calculated for a structure in the zigzag AFM (z-AFM) phase and for a structure in the nonmagnetic phase. The z-AFM phase is the low-temperature ground state (Supplementary Figure S9). In the z-AFM phase a 2 × 2 × 2 supercell is used with a 4 × 4 × 4 k-points grid. The phonon dispersion of the nonmagnetic (NM) phase uses a 4 × 4 × 1 supercell with a 6 × 6 × 1 k-points grid. The resulting dispersions are shown in Figure 4, and the frequencies are given in Table 1 (more details of calculated phonon modes in Table S1). The NM structure has a Raman inactive mode at 417 cm^{-1}, and the z-AFM structure shows a Raman inactive mode at 435 cm^{-1} which is in agreement with the P_2 peak observed by UV−Raman (Figure 3). The theoretical calculations in neither NM nor z-AFM structures do not show any phonon bands at the frequency range of that observed for P_3 = 467 cm^{-1}, confirming that this peak is most likely caused by a second-order Raman scattering process. The higher frequency Raman active mode for the NM structure is 526 cm^{-1} and for the z-AFM phase is 544−545 cm^{-1}, which are similar to frequencies previously calculated by others for a monolayer.[31] The atomic displacements of the Raman active mode are the same for both the NM and z-AFM simulations. All of the calculated dispersions and displacements are shown in the Supplementary Figures S10−S12 and Table S2. Note that in the phonon dispersion results of the AFM phase presented in Supplementary Figure S12a the number of irreducible representations is doubled by the lower symmetry in the modulated structure.

We investigated the evolution of Raman spectra of $FePS_3$ and $MnPS_3$ with temperature. The information on temperature coefficients of Raman modes can be used in the analysis of the crystal lattice anharmonicity and for extraction of the thermal data in the optothermal Raman method. This method has been widely used for measurements of the thermal conductivity of different free-standing and supported 2D materials.[8,38−41] It uses the Raman spectrometer both as a local heating element and as a thermometer. The measurement procedure involves three steps: temperature-dependent Raman measurements, excitation power-dependent measurements, and data extraction *via* iterative solution of the inverse heat diffusion problem. For the temperature dependent Raman measurements, the sample

https://dx.doi.org/10.1021/acsnano.9b09839
ACS Nano 2020, 14, 2424−2435

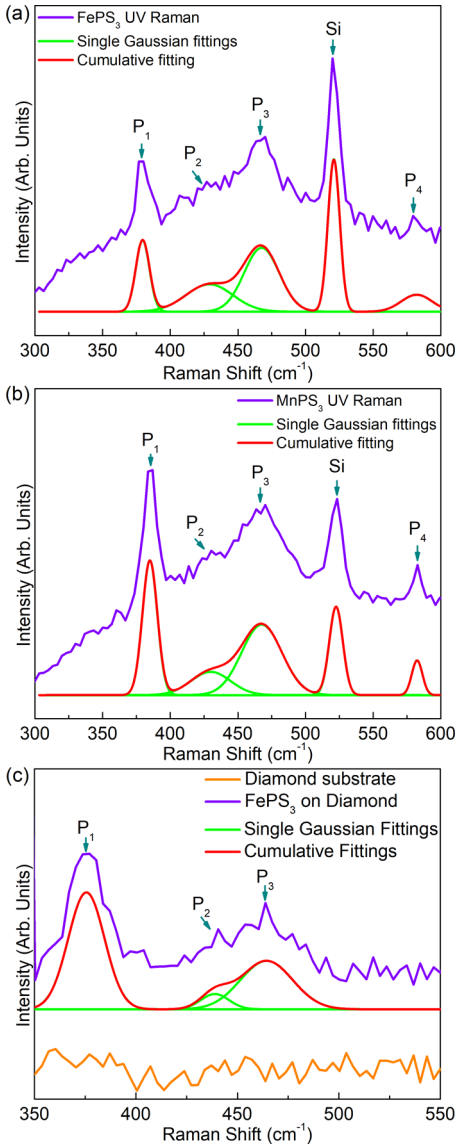

Figure 3. Raman spectroscopy of (a) $FePS_3$ and (b) $MnPS_3$ on silicon substrate and (c) $FePS_3$ on diamond substrate at room temperature using UV laser excitation wavelength. The violate curves are the experimental data. The green and red curves represent individual Gaussian and cumulative fittings to experimental data, respectively. The shoulder and peak identified as P_2 at ~430 cm^{-1} and P_3 at ~465 cm^{-1} are additional features which are only observable with UV laser excitation. The rest of the modes are detectable by red and blue laser excitation Raman spectroscopy as well. The peak marked as Si is associated with the silicon substrate.

is mounted in a hot−cold stage (Linkam Scientific, THMS-600), where its temperature can be controlled externally. The Raman measurements are conducted with the lowest possible laser excitation power of 39 μW at each individual sample temperature. The low laser power is essential at this step to avoid self-heating effects. However, it should be sufficient to achieve a reasonable signal-to-noise (S/N) ratio in the accumulated spectra.

The spectral positions of A_g Raman peaks of $FePS_3$ and $MnPS_3$ as a function of temperature, from RT to 350 K, are plotted in Figure 5a,b, respectively. The Raman spectra used to plot the dependence in Figure 5a,b are provided in Supplementary Figure S13a,b. For both crystals, the increase in temperature results in shifting of the A_g phonon peaks to lower frequencies. We used a linear fit to determine the Raman temperature coefficient, $\chi = d\omega/dT$. Here, ω is the frequency of the Raman A_g mode and T is the sample's temperature. One can see an excellent linear fit of the A_g Raman mode over the examined temperature range. The extracted Raman temperature coefficients are $\chi_{Fe} = -0.0154$ cm^{-1} K^{-1} and $\chi_{Mn} = -0.0108$ cm^{-1} K^{-1} with standard errors of 0.00156 cm^{-1} K^{-1} and 0.00178 cm^{-1} K^{-1} for $FePS_3$ and $MnPS_3$, respectively. One should note that the Raman temperature coefficients are different for each vibrational mode. Their value depends on the intrinsic material properties and the examined temperature range. In the optothermal Raman technique, the extracted thermal conductivity is independent of the specific peak chosen for the optothermal Raman analysis. In general, an intense narrow phonon peak with pronounced temperature dependence is preferred. In our case, the A_g Raman peaks of $FePS_3$ and $MnPS_3$ with Raman spectral positions of ~378 and ~383 cm^{-1} at RT satisfy these requirements.

The next step of the optothermal Raman measurements is to determine the spectral position of the A_g Raman mode as a function of increasing excitation laser power. The measurements were conducted at 633 nm wavelength (red laser). The laser power on the sample surface at each step was measured with a power meter (Newport 843-R). Increasing the excitation laser power results in the local laser-induced heating of the sample and the corresponding shift of the frequency of the Raman modes due to the local temperature rise. Figure 6a,b shows the measured A_g Raman shifts of $FePS_3$ and $MnPS_3$ as a function of the laser incident power, respectively. The A_g Raman mode of $FePS_3$ reveals a clear linear decrease in frequency with increasing the laser power, while for $MnPS_3$, the data are scattered. The power dependent Raman results depend on the optical properties of materials, *e.g.*, reflection and absorption coefficients of the material at the given laser wavelength. The absorption coefficient of $MnPS_3$ at the excitation laser wavelengths of 488 and 633 nm is less than 1200 cm^{-1},[2] which indicates that most of the light is not absorbed by the material and, thus, the sample experiences minor local heating by the incident laser light. For $FePS_3$, however, the absorption coefficient is ~12000 cm^{-1},[2] almost 10 times of that of $MnPS_3$, and therefore, the sample is heated strongly, exhibiting a clear Raman red-shift of the A_g phonon mode. The change in the frequency of the $FePS_3$ Raman A_g mode as a function of the incident laser power on the sample's surface (P_D) is defined as $\theta = d\omega/dP_D$ and found to be $\theta_{Fe} = -0.6723$ $cm^{-1}mW^{-1}$. The weak dependence of the $MnPS_3$ A_g Raman mode on laser power prevents its use for extracting thermal conductivity in the optothermal Raman method.

The final step of the Raman optothermal method is determining the thermal conductivity by solving the inverse heat-diffusion problem for the known geometry of the sample. The lateral dimensions and thickness of $FePS_3$ are determined from optical and AFM inspection (Supplementary Figures S2 and S3). The details of the thermal conductivity calculations are given in the Methods. Layered materials, such as $FePS_3$ and $MnPS_3$, have weak van der Waals forces between the layers along the "c" direction and strong covalent bonds among the in-plane "a" and "b" directions (the inset in Figure 1a). They are expected to have larger in-plane thermal conductivity ($k_{\parallel}$) and lower through-plane thermal conductivity ($k_{\perp}$). The Raman optothermal method used with the relatively thick or

https://dx.doi.org/10.1021/acsnano.9b09839
ACS Nano 2020, 14, 2424−2435

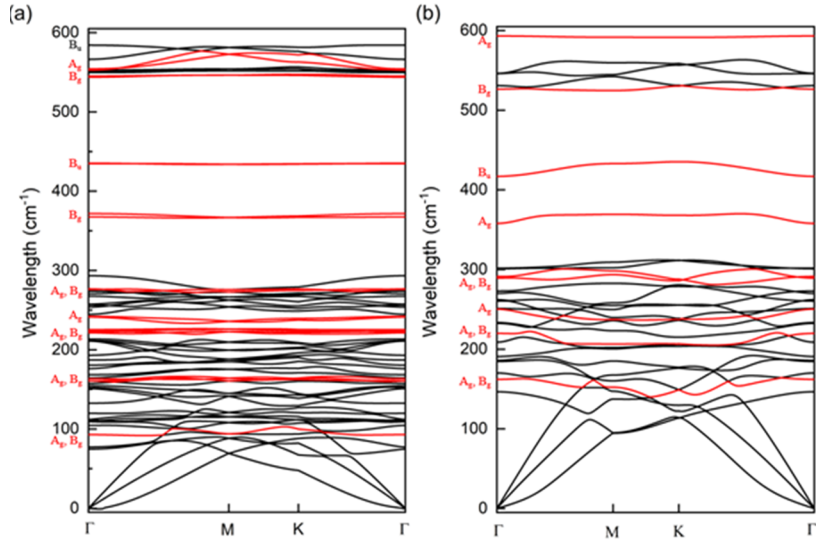

Figure 4. Calculated phonon dispersion of (a) modulated z-AFM $FePS_3$ and (b) nonmagnetic $FePS_3$.

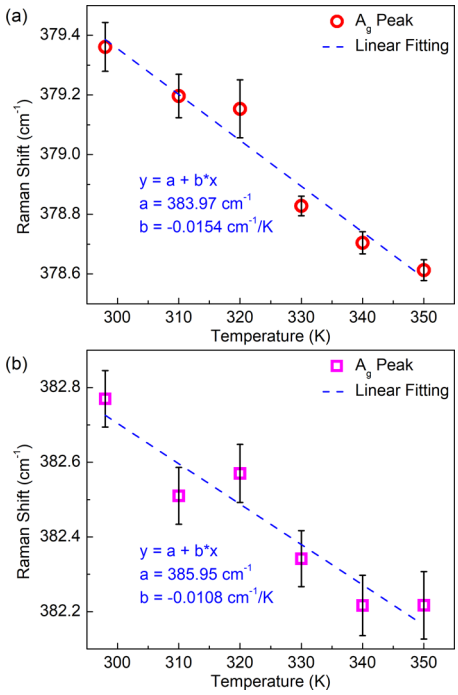

Figure 5. Raman A_{1g} peak of (a) $FePS_3$ and (b) $MnPS_3$ as a function of the sample temperature. The measurements were conducted at very low laser excitation power to avoid local heating. The peaks for both crystals exhibit a linear decrease in Raman shift with increasing the sample temperature. The obtained dependence is used as a calibration curve for the thermal conductivity measurements *via* optothermal Raman method.

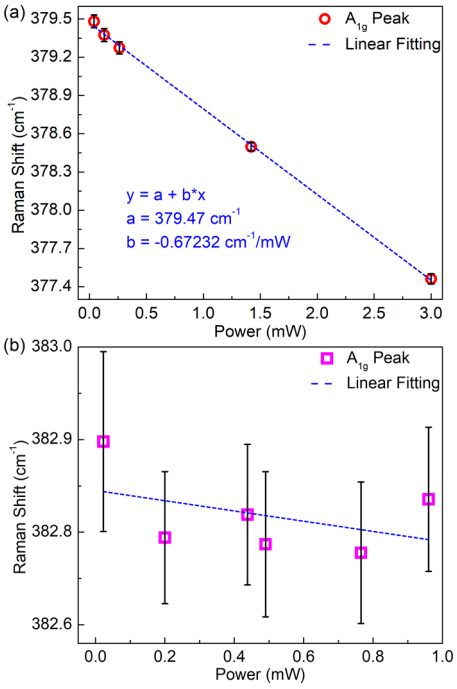

Figure 6. Raman A_{1g} peak of (a) $FePS_3$ and (b) $MnPS_3$ as a function of the laser excitation power. The samples were initially at room temperature. For $FePS_3$, the A_{1g} peak decrease linearly with increasing the laser power as a result of local heating. In $MnPS_3$, however, the change in Raman shift is within the errors of measurement due to the low absorption coefficient of $MnPS_3$ at laser excitation wavelength which prevents local heating of the sample.

bulk samples provides the directional average thermal conductivity, which has both in-plane and through-plane components. The thermal conductivity extraction procedure for $FePS_3$ is presented in Figure 7. A thermal conductivity of 1.35 ± 0.32 W m^{-1} K^{-1} was extracted for $FePS_3$ thin film with the thickness of 400 nm. Given the thickness range and smooth interface of the crystal one can assume that the phonon−boundary scattering does not play a significant role, and the extracted value can be considered as the average "bulk" thermal conductivity of $FePS_3$. The experimental uncertainty in the measured value is mostly associated with the uncertainty in determining the excitation laser spot size. It should be emphasized that the extracted thermal conductivity value is a weighted arithmetic mean of the through-plane ($k_\perp$) and in-plane thermal ($k_\parallel$) conductivities of $FePS_3$ as $k = \alpha k_\perp + \beta k_\parallel$ where α and β are the weight coefficients and thus $\alpha + \beta = 1$. On the basis of the lateral dimensions of the flake size (>10 μm) and the laser spot size (~1.5 μm), the extracted value by the optothermal Raman technique reflects more of the

https://dx.doi.org/10.1021/acsnano.9b09839
ACS Nano 2020, 14, 2424−2435

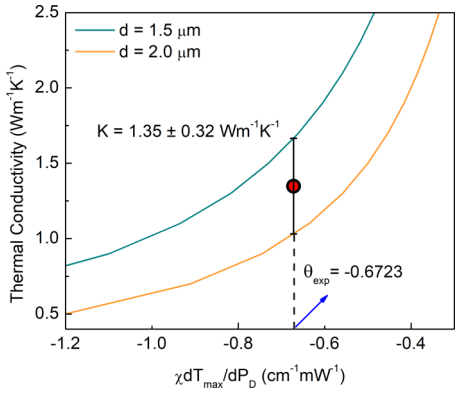

Figure 7. Numerical simulation of thermal conductivity of $FePS_3$ as a function of $\theta = \chi\, dT_{max}/dP_D$ using two different laser spot sizes. The dashed line presents θ as measured for $FePS_3$. The error bars exhibit the uncertainty in thermal conductivity calculations due to the uncertainty in laser spot size measurements. The extracted thermal conductivity is a weighted average of in-plane and cross-plane thermal conductivities of the crystal.

through-plane thermal conductivity rather than the in-plane thermal conductivity, *i.e.*, $\alpha > \beta$. This is confirmed by measuring the in-plane and through-plane thermal conductivities of both $FePS_3$ and $MnPS_3$ using TR-MOKE method as described below.

We determined separately the through-plane and in-plane thermal conductivity of the $MnPS_3$ and $FePS_3$ crystals with TR-MOKE measurements.[42−44] TR-MOKE is a pump/probe technique that determines thermal properties by measuring the transient evolution of the surface temperature that results from heating from pump pulses. The rate of thermal transport away from an optically heated surface depends strongly on the thermal conductivity tensor of the $MnPS_3$ or $FePS_3$ crystals. The TR-MOKE method is analogous to the more established technique known as the time-domain thermoreflectance (TDTR).[42−46] We chose to use TR-MOKE instead of TDTR to avoid coating the $MnPS_3$ and $FePS_3$ crystals with thick metal films. TDTR measurements require the sample of interest to be coated with an optically thick film, *e.g.*, 80 nm of Al. TR-MOKE experiments do not require an optically opaque film.[43,44] Using a thick metal film as a transducer in the current experiments would shunt the in-plane heat current and reduce our measurement's sensitivity to the in-plane thermal conductivity of $FePS_3$ and $MnPS_3$. TR-MOKE experiments require the sample be coated with a thin magnetic film. Therefore, we sputter coated the crystals with a ∼15 nm thick Pt and Co multilayer thin-film. The geometry of the multilayer was Ta (3 nm)/Pt (3 nm)/[Co (0.8 nm)/Pt (1 nm)] × 4/Pt (2 nm). The signals of interest in a TR-MOKE experiments are the in-phase and out-of-phase signals measured by a radio frequency lock-in at the modulation frequency of the pump beam, $V_{in}(t)$ and $V_{out}(t)$. We measure the in-phase and out-of-phase signals as a function of time-delay between the pump and probe pulses. The in-phase and out-of-phase signals are proportional to the temperature response of the metal film to heating by the pump pulse. A more detailed description of the TR-MOKE experiment and measured signals is contained in the Supporting Information and in refs 42−44. We analyze our experimental data, $V_{in}(t)/V_{out}(t)$, with a thermal model based on an analytical solution to the heat diffusion equation in cylindrical coordinates for a multilayer structure.[45]

In a TR-MOKE or TDTR experiment, the sensitivity to the substrate's in-plane *vs* through-plane thermal conductivity is determined by the pump modulation frequency, f_{mod}. The modulation frequency controls the thermal penetration depth, *i.e.*, the distance heat diffuses on the important time-scales of the experiment. At high frequencies, *e.g.*, 10 MHz, the thermal penetration depth is small compared to the laser spot-size, *e.g.*, 100 nm. As a result, the temperature gradients in the through-plane direction are much larger than those in the in-plane direction. In other words, at high modulation frequencies, the heat-transfer is one-dimensional in the through-plane direction. As a result, the ratio signal at 10 MHz has no sensitivity to the in-plane thermal conductivity. Alternatively, at low frequencies, *e.g.*, 1 MHz, the thermal penetration depth is comparable to the laser spot-size. As a result, heat-transfer is three-dimensional, and the measured signals depend on both $k_\perp$, and $k_\parallel$. In the Supporting Information, we quantify our measurement sensitivities to the various thermal properties of the sample (Supplementary Figure S14). Further details of the thermal model are in refs 47−49.

For each crystal, TR-MOKE measurements were performed with f_{mod} = 1 and 10 MHz. By fitting the data at multiple pump modulation frequencies with our thermal model, we determine all three unknown thermal properties of the sample stack: G, $k_\perp$, and $k_\parallel$. Here, $k_\perp$ and $k_\parallel$ represent the through-plane and average in-plane thermal conductivity of the crystal in axial and radial directions in cylindrical coordinates, respectively. We assume the in-plane thermal conductivity is the same in all radial directions.

In Figure 8, we plot our experimental data and the predictions of our thermal model. The values of $k_\perp$, and $k_\parallel$

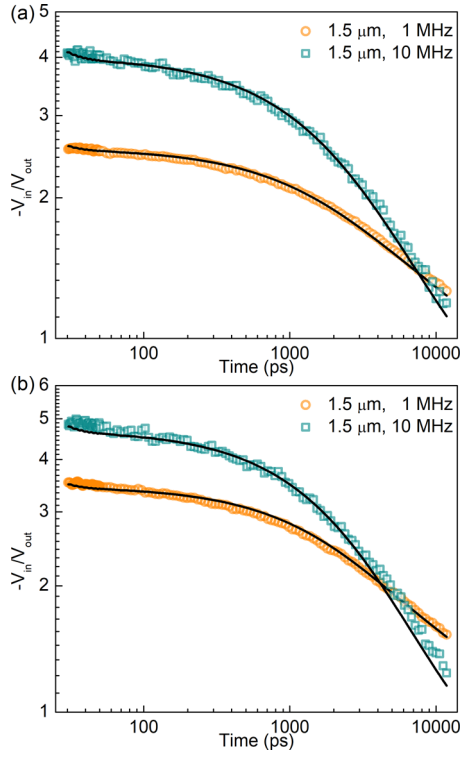

Figure 8. Time-resolved magneto-optic Kerr effect signals, $-V_{in}/V_{out}$ (open markers), and the best-fit curves (black lines) from the thermal model for the (a) [Co/Pt]/$FePS_3$ and (b) [Co/Pt]/$MnPS_3$ samples.

https://dx.doi.org/10.1021/acsnano.9b09839
ACS Nano 2020, 14, 2424−2435

Table 2. Summary of Through-Plane and In-Plane Thermal Conductivity of Similar Layered Materials

	thermal conductivity ($W\ m^{-1}\ K^{-1}$)				
material	k	$k_\perp$	$k_\parallel$	remarks	ref
$FePS_3$	1.35 ± 0.32	0.85 ± 0.15	2.7 ± 0.3	optothermal Raman and TR-MOKE (T = 300 K)	this work
$MnPS_3$		1.1 ± 0.2	6.3 ± 1.7	TR-MOKE (T = 300 K)	this work
$ZnPSe_3$	0.13			monolayer theory	18
1T-TaS_2	4.52			at 300 K	50,51
2H-$TaSe_2$	14.8			at 270 K	50
2H-$TaSe_2$	16			Raman	52
2H-$TaSe_2$	9			thin film, Raman	52
$HfTe_5$	5			parallel thermal conductance technique	53
MoS_2			82	time-domain thermoreflectance	54
MoS_2			16	steady-state heater setup at 300 K	55
MoS_2			52	few layers, Raman	56
MoS_2	55 ± 20		84 ± 17	monolayer, Raman, at 300 K	57
MoS_2	35 ± 7		77 ± 25	bilayer, Raman, at 300 K	57
MoS_2			34.5 ± 4	monolayer	39
MoS_2	1.05			pristine, laser flash, at 300 K	58
$MoSe_2$			35	time-domain thermoreflectance	54
$MoSe_2$	42 ± 13			bilayer	57
$MoSe_2$	24 ± 11		59 ± 18	monolayer, Raman, at 300 K	57
$MoSe_2$	17 ± 4		42 ± 13	bilayer, Raman, at 300 K	57
$MoSe_2$	0.85			pristine, laser flash, at 300 K	58
$NbSe_3$	0.24				59
$Ta_2Pd_3Se_8$	12.6			thermal bridge at 350 K	60
TiS_2	3.45			laser flash, at 300 K	61
TiS_3	3.5			laser flash at 325 K	62
TiS_3	3.7			laser flash at 325 K	63
WS_2			120	time-domain thermoreflectance	54
WS_2			32	monolayer, Raman at 300 K	64
WS_2			53	bilayer, Raman at 300 K	64
WS_2	2.2			pristine, laser flash, at 300 K	58
WSe_2			42	time-domain thermoreflectance	54
WSe_2	0.85			pristine, laser flash, at 300 K	58
WSe_2			1.5	thin film, at 300 K	65
$ZrTe_3$	7−7.5 (±5%)			polycrystalline, four terminal method, at 300 K	66
$ZrTe_5$	11.2			at 300 K	67
$ZrTe_5$	8			parallel thermal conductance technique	53
$ZrTe_5$	2			polycrystalline p-type, PPMS at 300 K	68

in the model were adjusted until the model predictions agreed with the experimental data. We find that the through-plane thermal conductivity of $FePS_3$ and $MnPS_3$ is 0.85 ± 0.15 W m^{-1} K^{-1} and 1.1 ± 0.2 W m^{-1} K^{-1}, respectively. The in-plane conductivity of $FePS_3$ and $MnPS_3$ is 2.7 ± 0.3 W m^{-1} K^{-1} and 6.3 ± 1.7 W m^{-1} K^{-1}. The interface conductance between the Ta seed-layer at the bottom of the metal multilayer and the $FePS_3$ and $MnPS_3$ crystals is 24 ± 4 MW m^{-2} K^{-1} and 23 ± 4 MW m^{-2} K^{-1}. Therefore, the interface provides an equivalent thermal resistance as ∼60 nm of amorphous glass. Thermally resistive interfaces between metals and 2D materials are common due to phonon focusing in the in-plane direction of the 2D material.[42] The obtained thermal conductivity values for $FePS_3$ and $MnPS_3$ and other similar layered materials are summarized in Table 2.

CONCLUSIONS

In this study, we investigated the phonon and thermal conductivity properties of high-quality single crystals of $FePS_3$ and $MnPS_3$ using Raman spectroscopy, optothermal Raman, and TR-MOKE experimental techniques at room temperature. The Raman spectra were excited with three different laser excitation wavelengths of 325, 488, and 633 nm. The data obtained by UV−Raman revealed additional spectral features, which have not been previously detected with regular visible-light Raman spectroscopy. An optothermal Raman technique was used to extract the directional average thermal conductivity of bulk $FePS_3$. The data extraction was based on the results of the frequency changes of the main A_g Raman mode as a function of temperature and excitation laser power. The directional average "bulk" thermal conductivity of $FePS_3$ was determined to be k = 1.35 ± 0.32 W m^{-1} K^{-1}. This value represents a weighted average of the in-plane and through-plane thermal conductivities of the crystal according to $k = \alpha k_\perp + \beta k_\parallel$ in which $\alpha + \beta = 1$ and $\alpha > \beta$. We conducted TR-MOKE measurements in order to determine the anisotropic thermal properties of both $FePS_3$ and $MnPS_3$ bulk crystals. The experiments revealed in-plane thermal conductivity of 2.7 ± 0.3 W m^{-1} K^{-1} and 6.3 ± 1.7 W m^{-1} K^{-1} for $FePS_3$ and $MnPS_3$, respectively. The through-plane thermal conductivity measurements reported 0.85 ± 0.15 and 1.1 ± 0.2 W m^{-1} K^{-1} for $FePS_3$ and $MnPS_3$. Comparing the in-plane and cross-plane thermal conductivity values of $FePS_3$ obtained by TR-MOKE measurements with that of attained *via* the optothermal Raman

https://dx.doi.org/10.1021/acsnano.9b09839
ACS Nano 2020, 14, 2424−2435

technique with isotropic assumption, the weighted coefficients of α and β are calculated as 0.73 and 0.27, respectively. The obtained results are important for understanding the phonon properties and phonon transport in layered antiferromagnetic semiconductors as well as for their applications in spintronic and caloritronic devices.

METHODS

Thermal Conductivity Extraction *via* Optothermal Method. We utilized the COMSOL software package in order to solve the steady-state Fourier heat equation $\nabla(\kappa\nabla T) + q''' = 0$ using the finite element method. In this equation, T is the temperature distribution of the system and q''' is the laser heat source which can be defined using a Gaussian distribution function as $q''' = \frac{(1-R)P_D\alpha}{(2\pi\sigma^2)}\exp\left(-\frac{x^2+y^2}{2\sigma^2}\right)\exp(-\alpha|z|)$, respectively. Here, x, y, z are the Cartesian coordinates, P_D is the total laser power at the center of the sample's surface ($x = y = z = 0$), and R and α are the sample's reflection and absorption coefficients at the laser excitation wavelength, respectively. The standard deviation of the Gaussian power (σ) is calculated as $\sigma = r/2$ where r is the radius of the laser spot on sample's surface. The laser spot size should be measured experimentally using the knife-edge method.[69] The lateral dimensions and thickness of $FePS_3$ are extracted by careful imaging of the flake using optical and atomic force microscopy (AFM). The simulated structure from top to bottom corresponds to a 400 nm thick $FePS_3$ flake, 300 nm SiO_2 layer, and 4 μm silicon substrate. In order to extract the thermal conductivity, a reiterative procedure was followed. In this model, first a thermal conductivity for the material system is assumed and then the temperature distribution is obtained solving the heat diffusion equation using COMSOL software assuming different values of incident power (P_D). At each assumed thermal conductivity value, $\frac{\partial T_{max}}{\partial P_D}$ and then $\theta = \chi_{Fe}\frac{\partial T_{max}}{\partial P_D}$ are calculated. The maximum temperature (T_{max}) is obtained from the simulations. The temperature coefficient, χ_{Fe}, was obtained *via* linear fitting of the experimental Raman peak shift as a function of temperature. Finally, the thermal conductivity is plotted as a function of θ and compared to the experimental value ($\theta_{exp} = d\omega/dP_D$) which is obtained by linear fitting of Raman peak shift as a function of temperature.

ASSOCIATED CONTENT

Supporting Information

The Supporting Information is available free of charge at https://pubs.acs.org/doi/10.1021/acsnano.9b09839.

detailed description of sample characterizations, optical microscopy and atomic force microscopy, UV−Raman spectroscopy of different flakes of $FePS_3$ and $MnPS_3$, bare silicon, and diamond substrates, density functional theory calculations and atomic displacement of optical phonon modes, temperature dependent visible Raman data, TR-MOKE experimental technique, and sensitivity analyses of the extracted thermal conductivity values (PDF)

AUTHOR INFORMATION

Corresponding Authors

Fariborz Kargar − *Phonon Optimized Engineered Materials (POEM) Center, Department of Electrical and Computer Engineering, University of California, Riverside, California 92521, United States;* orcid.org/0000-0003-2192-2023; Email: fkargar@engr.ucr.edu

Alexander A. Balandin − *Phonon Optimized Engineered Materials (POEM) Center, Department of Electrical and Computer Engineering and Spins and Heat in Nanoscale Electronic Systems (SHINES) Center, University of California, Riverside, California 92521, United States*; Email: balandin@ece.ucr.edu; http://balandingroup.ucr.edu/

Authors

Ece A. Coleman − *Phonon Optimized Engineered Materials (POEM) Center, Department of Electrical and Computer Engineering, University of California, Riverside, California 92521, United States*

Subhajit Ghosh − *Phonon Optimized Engineered Materials (POEM) Center, Department of Electrical and Computer Engineering, University of California, Riverside, California 92521, United States*

Jonathan Lee − *Mechanical Engineering Department and Materials Science and Engineering Program, University of California, Riverside, California 92521, United States*

Michael J. Gomez − *Mechanical Engineering Department and Materials Science and Engineering Program, University of California, Riverside, California 92521, United States*

Yuhang Liu − *Laboratory for Terascale and Terahertz Electronics (LATTE), Department of Electrical and Computer Engineering, University of California, Riverside, California 92521, United States*

Andres Sanchez Magana − *Phonon Optimized Engineered Materials (POEM) Center, Department of Electrical and Computer Engineering, University of California, Riverside, California 92521, United States*

Zahra Barani − *Phonon Optimized Engineered Materials (POEM) Center, Department of Electrical and Computer Engineering, University of California, Riverside, California 92521, United States*

Amirmahdi Mohammadzadeh − *Phonon Optimized Engineered Materials (POEM) Center, Department of Electrical and Computer Engineering, University of California, Riverside, California 92521, United States*

Bishwajit Debnath − *Laboratory for Terascale and Terahertz Electronics (LATTE), Department of Electrical and Computer Engineering, University of California, Riverside, California 92521, United States*

Richard B. Wilson − *Mechanical Engineering Department and Materials Science and Engineering Program and Spins and Heat in Nanoscale Electronic Systems (SHINES) Center, University of California, Riverside, California 92521, United States*

Roger K. Lake − *Laboratory for Terascale and Terahertz Electronics (LATTE), Department of Electrical and Computer Engineering and Spins and Heat in Nanoscale Electronic Systems (SHINES) Center, University of California, Riverside, California 92521, United States*

Complete contact information is available at: https://pubs.acs.org/10.1021/acsnano.9b09839

Author Contributions

A.A.B., E.A.C., and F.K. conceived the idea of the study. A.A.B. coordinated the project and contributed to the experimental and theoretical data analysis; E.A.C. carried out the visible light Raman measurements and contributed to the data analysis; F.K. coordinated Raman data analysis and performed numerical simulations; S.G. conducted UV−Raman measurements; M.J.G. and J.L. carried out and analyzed the TR-MOKE measurements under the supervision of R.W.; A.S.M. conducted sample characterization; Z.B. and A.M. contributed to temperature dependent Raman measurements; Y.L. performed the DFT calculations of the vibrational modes.

https://dx.doi.org/10.1021/acsnano.9b09839
ACS Nano 2020, 14, 2424−2435

B.D. contributed to numerical modeling and thermal conductivity extraction; R.K.L. supervised the theory and modeling. F.K. and A.A.B. led the manuscript preparation. All authors contributed to writing and editing of the manuscript.

Author Contributions

[#]F.K. and E.A.C. contributed equally to the work.

Notes

The authors declare no competing financial interest.

An initial draft of the paper prior to acceptance to ACS Nano was uploaded on *arXiv* repository previously.[71]

ACKNOWLEDGMENTS

The work at UC Riverside was supported as part of the Spins and Heat in Nanoscale Electronic Systems (SHINES), an Energy Frontier Research Center funded by the U.S. Department of Energy, Office of Science, Basic Energy Sciences (BES) under Award No. SC0012670. The authors thank D. Yang at UC Riverside Center for Nanoscale Science and Engineering for his help with sample characterization. This work used the Extreme Science and Engineering Discovery Environment (XSEDE),[70] which is supported by National Science Foundation Grant No. ACI-1548562 and allocation ID TG-DMR130081.

REFERENCES

(1) Chittari, B. L.; Park, Y.; Lee, D.; Han, M.; Macdonald, A. H.; Hwang, E.; Jung, J. Electronic and Magnetic Properties of Single-Layer MPX_3 Metal Phosphorous Trichalcogenides. *Phys. Rev. B: Condens. Matter Mater. Phys.* **2016**, *94*, 184428.

(2) Brec, R.; Schleich, D. M.; Ouvrard, G.; Louisy, A.; Rouxel, J. Physical Properties of Lithium Intercalation Compounds of the Layered Transition-Metal Chalcogenophosphites. *Inorg. Chem.* **1979**, *18*, 1814−1818.

(3) Fujii, Y.; Miura, A.; Rosero-Navarro, N. C.; Higuchi, M.; Tadanaga, K. $FePS_3$ Electrodes in All-Solid-State Lithium Secondary Batteries Using Sulfide-Based Solid Electrolytes. *Electrochim. Acta* **2017**, *241*, 370−374.

(4) Geim, A. K.; Novoselov, K. S. The Rise of Graphene. *Nat. Mater.* **2007**, *6*, 183−191.

(5) Novoselov, K. S.; Geim, A. K.; Morozov, S. V.; Jiang, D.; Zhang, Y.; Dubonos, S. V.; Grigorieva, I. V.; Firsov, A. A. Electric Field Effect in Atomically Thin Carbon Films. *Science* **2004**, *306*, 666−669.

(6) Novoselov, K. S.; Geim, A. K.; Morozov, S. V.; Jiang, D.; Katsnelson, M. I.; Grigorieva, I. V.; Dubonos, S. V.; Firsov, A. A. Two-Dimensional Gas of Massless Dirac Fermions in Graphene. *Nature* **2005**, *438*, 197−200.

(7) Berger, C.; Song, Z.; Li, T.; Li, X.; Ogbazghi, A. Y.; Feng, R.; Dai, Z.; Marchenkov, A. N.; Conrad, E. H.; First, P. N.; de Heer, W. A. Ultrathin Epitaxial Graphite: 2D Electron Gas Properties and a Route toward Graphene-Based Nanoelectronics. *J. Phys. Chem. B* **2004**, *108*, 19912−19916.

(8) Balandin, A. A.; Ghosh, S.; Bao, W.; Calizo, I.; Teweldebrhan, D.; Miao, F.; Lau, C. N. Superior Thermal Conductivity of Single-Layer Graphene. *Nano Lett.* **2008**, *8*, 902−907.

(9) Balandin, A. A. Thermal Properties of Graphene and Nanostructured Carbon Materials. *Nat. Mater.* **2011**, *10*, 569−581.

(10) Bonilla, M.; Kolekar, S.; Ma, Y.; Diaz, H. C.; Kalappattil, V.; Das, R.; Eggers, T.; Gutierrez, H. R.; Phan, M.-H.; Batzill, M. Strong Room-Temperature Ferromagnetism in VSe_2 Monolayers on van der Waals Substrates. *Nat. Nanotechnol.* **2018**, *13*, 289−293.

(11) O'Hara, D. J.; Zhu, T.; Trout, A. H.; Ahmed, A. S.; Luo, Y. K.; Lee, C. H.; Brenner, M. R.; Rajan, S.; Gupta, J. A.; McComb, D. W.; Kawakami, R. K. Room Temperature Intrinsic Ferromagnetism in Epitaxial Manganese Selenide Films in the Monolayer Limit. *Nano Lett.* **2018**, *18*, 3125−3131.

(12) Lee, J. U.; Lee, S.; Ryoo, J. H.; Kang, S.; Kim, T. Y.; Kim, P.; Park, C. H.; Park, J. G.; Cheong, H. Ising-Type Magnetic Ordering in Atomically Thin $FePS_3$. *Nano Lett.* **2016**, *16*, 7433−7438.

(13) Du, K.; Wang, X.; Liu, Y.; Hu, P.; Utama, M. I. B.; Gan, C. K.; Xiong, Q.; Kloc, C. Weak van der Waals Stacking, Wide-Range Band Gap, and Raman Study on Ultrathin Layers of Metal Phosphorus Trichalcogenides. *ACS Nano* **2016**, *10*, 1738−1743.

(14) Wang, F.; Shifa, T. A.; Yu, P.; He, P.; Liu, Y.; Wang, F.; Wang, Z.; Zhan, X.; Lou, X.; Xia, F.; He, J. New Frontiers on van der Waals Layered Metal Phosphorous Trichalcogenides. *Adv. Funct. Mater.* **2018**, *28*, 1802151.

(15) Wu, S. M.; Zhang, W.; Kc, A.; Borisov, P.; Pearson, J. E.; Jiang, J. S.; Lederman, D.; Hoffmann, A.; Bhattacharya, A. Antiferromagnetic Spin Seebeck Effect. *Phys. Rev. Lett.* **2016**, *116*, 097204.

(16) Boona, S. R.; Myers, R. C.; Heremans, J. P. Spin Caloritronics. *Energy Environ. Sci.* **2014**, *7*, 885−910.

(17) Kumar, R.; Jenjeti, R. N.; Austeria, M. P.; Sampath, S. Bulk and Few-Layer $MnPS_3$: A New Candidate for Field Effect Transistors and UV Photodetectors. *J. Mater. Chem. C* **2019**, *7*, 324−329.

(18) Yun, W. S.; Lee, J. D. Exploring a Novel Atomic Layer with Extremely Low Lattice Thermal Conductivity: $ZnPSe_3$ and Its Thermoelectrics. *J. Phys. Chem. C* **2018**, *122*, 27917−27924.

(19) Shifa, T. A.; Wang, F.; Cheng, Z.; He, P.; Liu, Y.; Jiang, C.; Wang, Z.; He, J. High Crystal Quality 2D Manganese Phosphorus Trichalcogenide Nanosheets and Their Photocatalytic Activity. *Adv. Funct. Mater.* **2018**, *28*, 1800548.

(20) ur Rehman, Z.; Muhammad, Z.; Adetunji Moses, O.; Zhu, W.; Wu, C.; He, Q.; Habib, M.; Song, L. Magnetic Isotropy/Anisotropy in Layered Metal Phosphorous Trichalcogenide MPS_3 (M = Mn, Fe) Single Crystals. *Micromachines* **2018**, *9*, 292.

(21) Wang, X.; Song, Z.; Wen, W.; Liu, H.; Wu, J.; Dang, C.; Hossain, M.; Iqbal, M. A.; Xie, L. *Potential 2D Materials with Phase Transitions: Structure, Synthesis, and Device Applications. Advanced Materials*; John Wiley & Sons, Ltd., 2018; p 1804682.

(22) Sun, Y. J.; Tan, Q. H.; Liu, X. L.; Gao, Y. F.; Zhang, J. Probing the Magnetic Ordering of Antiferromagnetic $MnPS_3$ by Raman Spectroscopy. *J. Phys. Chem. Lett.* **2019**, *10*, 3087−3093.

(23) Kim, K.; Lim, S. Y.; Lee, J. U.; Lee, S.; Kim, T. Y.; Park, K.; Jeon, G. S.; Park, C. H.; Park, J. G.; Cheong, H. Suppression of Magnetic Ordering in XXZ-Type Antiferromagnetic Monolayer $NiPS_3$. *Nat. Commun.* **2019**, *10*, 345.

(24) Scagliotti, M.; Jouanne, M.; Balkanski, M.; Ouvrard, G. Spin Dependent Phonon Raman Scattering in Antiferromagnetic $FePS_3$ Layer-Type Compound. *Solid State Commun.* **1985**, *54*, 291−294.

(25) Scagliotti, M.; Jouanne, M.; Balkanski, M.; Ouvrard, G.; Benedek, G. Raman Scattering in Antiferromagnetic $FePS_3$ and $FePSe_3$ Crystals. *Phys. Rev. B: Condens. Matter Mater. Phys.* **1987**, *35*, 7097−7104.

(26) Bernasconi, M.; Marra, G. L.; Benedek, G.; Miglio, L.; Jouanne, M.; Julien, C.; Scagliotti, M.; Balkanski, M. Lattice Dynamics of Layered MPX_3 (M = Mn,Fe,Ni,Zn; X = S,Se) Compounds. *Phys. Rev. B: Condens. Matter Mater. Phys.* **1988**, *38*, 12089−12099.

(27) Sekine, T.; Jouanne, M.; Julien, C.; Balkanski, M. Light-Scattering Study of Dynamical Behavior of Antiferromagnetic Spins in the Layered Magnetic Semiconductor $FePS_3$. *Phys. Rev. B: Condens. Matter Mater. Phys.* **1990**, *42*, 8382−8393.

(28) Joy, P. A.; Vasudevan, S. Infrared (700−100 cm^{-1}) Vibrational Spectra of the Layered Transition Metal Thiophosphates, MPS_3 (M = Mn, Fe and Ni). *J. Phys. Chem. Solids* **1993**, *54*, 343−348.

(29) Balkanski, M.; Jouanne, M.; Scagliotti, M. Magnetic Ordering Induced Raman Scattering in $FePS_3$ and $NiPS_3$ Layered Compounds. *Pure Appl. Chem.* **1987**, *59*, 1247−1252.

(30) Wang, X.; Du, K.; Liu, Y. Y. F.; Hu, P.; Zhang, J.; Zhang, Q.; Owen, M. H. S.; Lu, X.; Gan, C. K.; Sengupta, P.; Kloc, C.; Xiong, Q. Raman Spectroscopy of Atomically Thin Two-Dimensional Magnetic Iron Phosphorus Trisulfide ($FePS_3$) Crystals. *2D Mater.* **2016**, *3*, 031009.

(31) Hashemi, A.; Komsa, H.-P.; Puska, M.; Krasheninnikov, A. V. Vibrational Properties of Metal Phosphorus Trichalcogenides from

https://dx.doi.org/10.1021/acsnano.9b09839
ACS Nano 2020, 14, 2424−2435

First-Principles Calculations. *J. Phys. Chem. C* **2017**, *121*, 27207−27217.
(32) Takashima, R.; Shiomi, Y.; Motome, Y. Nonreciprocal Spin Seebeck Effect in Antiferromagnets. *Phys. Rev. B: Condens. Matter Mater. Phys.* **2018**, *98*, No. 020401.
(33) Semenova, L. E.; Prokhorov, K. A. Theoretical Treatment of the Second-Order Raman Scattering. *Laser Phys.* **2007**, *17*, 824−830.
(34) Kresse, G.; Furthmüller, J. Efficiency of *Ab Initio* Total Energy Calculations for Metals and Semiconductors Using a Plane-Wave Basis Set. *Comput. Mater. Sci.* **1996**, *6*, 15−50.
(35) Kresse, G.; Hafner, J. *Ab Initio* Molecular Dynamics for Open-Shell Transition Metals. *Phys. Rev. B: Condens. Matter Mater. Phys.* **1993**, *48*, 13115−13118.
(36) Perdew, J. P.; Burke, K.; Ernzerhof, M. Generalized Gradient Approximation Made Simple. *Phys. Rev. Lett.* **1996**, *77*, 3865−3868.
(37) Grimme, S. Semiempirical GGA-Type Density Functional Constructed with a Long-Range Dispersion Correction. *J. Comput. Chem.* **2006**, *27*, 1787−1799.
(38) Cai, W.; Moore, A. L.; Zhu, Y.; Li, X.; Chen, S.; Shi, L.; Ruoff, R. S. Thermal Transport in Suspended and Supported Monolayer Graphene Grown by Chemical Vapor Deposition. *Nano Lett.* **2010**, *10*, 1645−1651.
(39) Yan, R.; Simpson, J. R.; Bertolazzi, S.; Brivio, J.; Watson, M.; Wu, X.; Kis, A.; Luo, T.; Hight Walker, A. R.; Xing, H. G. Thermal Conductivity of Monolayer Molybdenum Disulfide Obtained from Temperature-Dependent Raman Spectroscopy. *ACS Nano* **2014**, *8*, 986−993.
(40) Yan, Z.; Liu, G.; Khan, J. M.; Balandin, A. A. Graphene Quilts for Thermal Management of High-Power GaN Transistors. *Nat. Commun.* **2012**, *3*, 827.
(41) Peimyoo, N.; Shang, J.; Yang, W.; Wang, Y.; Cong, C.; Yu, T. Thermal Conductivity Determination of Suspended Mono- and Bilayer WS_2 by Raman Spectroscopy. *Nano Res.* **2015**, *8*, 1210−1221.
(42) Kimling, J.; Kimling, J.; Wilson, R. B.; Hebler, B.; Albrecht, M.; Cahill, D. G. Ultrafast Demagnetization of FePt:Cu Thin Films and the Role of Magnetic Heat Capacity. *Phys. Rev. B: Condens. Matter Mater. Phys.* **2014**, *90*, 224408.
(43) Jiang, P.; Qian, X.; Yang, R. Tutorial: Time-Domain Thermoreflectance (TDTR) for Thermal Property Characterization of Bulk and Thin Film Materials. *J. Appl. Phys.* **2018**, *124*, 161103.
(44) Zhu, J.; Park, H.; Chen, J.-Y.; Gu, X.; Zhang, H.; Karthikeyan, S.; Wendel, N.; Campbell, S. A.; Dawber, M.; Du, X.; Li, M.; Wang, J.-P.; Yang, R.; Wang, X. Revealing the Origins of 3D Anisotropic Thermal Conductivities of Black Phosphorus. *Adv. Electron. Mater.* **2016**, *2*, 1600040.
(45) Cahill, D. G.; Braun, P. V.; Chen, G.; Clarke, D. R.; Fan, S.; Goodson, K. E.; Keblinski, P.; King, W. P.; Mahan, G. D.; Majumdar, A.; Maris, H. J.; Phillpot, S. R.; Pop, E.; Shi, L. Nanoscale Thermal Transport. II. 2003−2012. *Appl. Phys. Rev.* **2014**, *1*, 11305.
(46) Wilson, R. B.; Apgar, B. A.; Martin, L. W.; Cahill, D. G. Thermoreflectance of Metal Transducers for Optical Pump-Probe Studies of Thermal Properties. *Opt. Express* **2012**, *20*, 28829.
(47) Cahill, D. G. Analysis of Heat Flow in Layered Structures for Time-Domain Thermoreflectance. *Rev. Sci. Instrum.* **2004**, *75*, 5119−5122.
(48) Feser, J. P.; Liu, J.; Cahill, D. G. Pump-Probe Measurements of the Thermal Conductivity Tensor for Materials Lacking In-Plane Symmetry. *Rev. Sci. Instrum.* **2014**, *85*, 104903.
(49) Schmidt, A. J.; Chen, X.; Chen, G. Pulse Accumulation, Radial Heat Conduction, and Anisotropic Thermal Conductivity in Pump-Probe Transient Thermoreflectance. *Rev. Sci. Instrum.* **2008**, *79*, 114902.
(50) Núñez-Regueiro, M. D.; Lopez-Castillo, J. M.; Ayache, C. Thermal Conductivity of 1T-TaS_2 and 2H-$TaSe_2$. *Phys. Rev. Lett.* **1985**, *55*, 1931−1934.
(51) Balaguru Rayappan, J. B.; Raj, S. A. C.; Lawrence, N. Thermal Properties of 1T-TaS_2 at the Onset of Charge Density Wave States. *Phys. B* **2010**, *405*, 3172−3175.
(52) Yan, Z.; Jiang, C.; Pope, T. R.; Tsang, C. F.; Stickney, J. L.; Goli, P.; Renteria, J.; Salguero, T. T.; Balandin, A. A. Phonon and Thermal Properties of Exfoliated $TaSe_2$ Thin Films. *J. Appl. Phys.* **2013**, *114*, 204301.
(53) Zawilski, B. M.; Littleton IV, R. T.; Tritt, T. M. Investigation of the Thermal Conductivity of the Mixed Pentatellurides $Hf_{1-X}Zr_xTe_5$. *Appl. Phys. Lett.* **2000**, *77*, 2319−2321.
(54) Jiang, P.; Qian, X.; Gu, X.; Yang, R. Probing Anisotropic Thermal Conductivity of Transition Metal Dichalcogenides MX_2 (M = Mo, W and X = S, Se) Using Time-Domain Thermoreflectance. *Adv. Mater.* **2017**, *29*, 1701068.
(55) Pisoni, A.; Jacimovic, J.; Barišic, O. S.; Walter, A.; Náfrádi, B.; Bugnon, P.; Magrez, A.; Berger, H.; Revay, Z.; Forró, L. The Role of Transport Agents in MoS_2 Single Crystals. *J. Phys. Chem. C* **2015**, *119*, 3918−3922.
(56) Sahoo, S.; Gaur, A. P. S.; Ahmadi, M.; Guinel, M. J. F.; Katiyar, R. S. Temperature-Dependent Raman Studies and Thermal Conductivity of Few-Layer MoS_2. *J. Phys. Chem. C* **2013**, *117*, 9042−9047.
(57) Zhang, X.; Sun, D.; Li, Y.; Lee, G. H.; Cui, X.; Chenet, D.; You, Y.; Heinz, T. F.; Hone, J. C. Measurement of Lateral and Interfacial Thermal Conductivity of Single- and Bilayer MoS_2 and $MoSe_2$ Using Refined Optothermal Raman Technique. *ACS Appl. Mater. Interfaces* **2015**, *7*, 25923−25929.
(58) Kim, J.-Y.; Choi, S.-M.; Seo, W.-S.; Cho, W.-S. Thermal and Electronic Properties of Exfoliated Metal Chalcogenides. *Bull. Korean Chem. Soc.* **2010**, *31*, 3225−3227.
(59) Brill, J. W.; Tzou, C. P.; Verma, G.; Ong, N. P. Thermal Conductivity of $NbSe_3$. *Solid State Commun.* **1981**, *39*, 233−237.
(60) Zhang, Q.; Liu, C.; Liu, X.; Liu, J.; Cui, Z.; Zhang, Y.; Yang, L.; Zhao, Y.; Xu, T. T.; Chen, Y.; Wei, J.; Mao, Z.; Li, D. Thermal Transport in Quasi-1D van der Waals Crystal $Ta_2Pd_3Se_8$ Nanowires: Size and Length Dependence. *ACS Nano* **2018**, *12*, 2634−2642.
(61) Guilmeau, E.; Bréard, Y.; Maignan, A. Transport and Thermoelectric Properties in Copper Intercalated TiS_2 Chalcogenide. *Appl. Phys. Lett.* **2011**, *99*, 52107.
(62) Misse, P. R. N.; Berthebaud, D.; Lebedev, O. I.; Maignan, A.; Guilmeau, E. Synthesis and Thermoelectric Properties in the 2D $Ti_{1-x}Nb_xS_3$ Trichalcogenides. *Materials* **2015**, *8*, 2514−2522.
(63) Guilmeau, E.; Berthebaud, D.; Misse, P. R. N.; Hébert, S.; Lebedev, O. I.; Chateigner, D.; Martin, C.; Maignan, A. $ZrSe_3$-Type Variant of TiS_3: Structure and Thermoelectric Properties. *Chem. Mater.* **2014**, *26*, 5585−5591.
(64) Peimyoo, N.; Shang, J.; Yang, W.; Wang, Y.; Cong, C.; Yu, T. Thermal Conductivity Determination of Suspended Mono- and Bilayer WS_2 by Raman Spectroscopy. *Nano Res.* **2015**, *8*, 1210−1221.
(65) Mavrokefalos, A.; Nguyen, N. T.; Pettes, M. T.; Johnson, D. C.; Shi, L. In-Plane Thermal Conductivity of Disordered Layered WSe_2 and $(W)_x(WSe_2)_y$ Superlattice Films. *Appl. Phys. Lett.* **2007**, *91*, 171912.
(66) Hooda, M. K.; Tripathi, T. S.; Yadav, C. S. Semiconducting Nature and Thermal Transport Studies of $ZrTe_3$. *J. Alloys Compd.* **2019**, *785*, 603−609.
(67) Smontara, A.; Biljaković, K. Thermal Properties of $ZrTe_5$. *Mol. Cryst. Liq. Cryst.* **1985**, *121*, 141−144.
(68) Hooda, M. K.; Yadav, C. S. Enhanced Thermopower and Low Thermal Conductivity in *p*-Type Polycrystalline $ZrTe_5$. *Appl. Phys. Lett.* **2017**, *111*, 053902.
(69) Suzaki, Y.; Tachibana, A. Measurement of the μm Sized Radius of Gaussian Laser Beam Using the Scanning Knife-Edge. *Appl. Opt.* **1975**, *14*, 2809.
(70) Towns, J.; Cockerill, T.; Dahan, M.; Foster, I.; Gaither, K.; Grimshaw, A.; Hazlewood, V.; Lathrop, S.; Lifka, D.; Peterson, G. D.; Roskies, R.; Scott, J. R.; Wilkens-Diehr, N. XSEDE: Accelerating Scientific Discovery. *Comput. Sci. Eng.* **2014**, *16*, 62−74.
(71) Kargar, F.; Aytan, E.; Ghosh, S.; Lee, J.; Gomez, M.; Liu, Y.; Magana, A. S.; Beiranvand, Z. B.; Debnath, B.; Wilson, R.; Lake, R. K.; Balandin, A. A. Phonon and Thermal Properties of Quasi-Two-

https://dx.doi.org/10.1021/acsnano.9b09839
ACS Nano 2020, 14, 2424−2435

Dimensional $FePS_3$ and $MnPS_3$ Antiferromagnetic Semiconductor Materials. *arXiv* **2019**, 1908.05186. https://arxiv.org/abs/1908.05186

https://dx.doi.org/10.1021/acsnano.9b09839
ACS Nano 2020, 14, 2424−2435